# On understanding microstructure and inclusion effects on machinability of additively manufactured 316L stainless steel



Citation for the original published paper (version of record):
Hoier, P., Malladi, B., Mallipeddi, D. et al (2026). On understanding microstructure and inclusion effects on machinability of additively
manufactured 316L stainless steel. Journal of Manufacturing Processes, 175: 315-329.
http://dx.doi.org/10.1016/j.jmapro.2026.08.017

Journal of Manufacturing Processes 175 (2026) 315–329

Contents lists available at ScienceDirect

Journal of Manufacturing Processes

journal homepage: www.elsevier.com/locate/manpro

# On understanding microstructure and inclusion effects on machinability of additively manufactured 316L stainless steel

Philipp Hoier *, Sri Bala Aditya Malladi, Dinesh Mallipeddi, Lars Nyborg, Peter Krajnik

*Department of Mechanical Engineering, Chalmers University of Technology, Gothenburg, Sweden*

## HIGHLIGHTS

- Microstructure-machinability link established for AM and wrought 316 L steels.
- EBSD and EDS reveal hierarchical grains, dislocations and inclusions in AM 316 L.
- AM 316 L shows similar cutting forces but significantly accelerated flank wear.
- Oxide-rich, MnS-free AM microstructures increase abrasive wear on cutting tools.
- Inclusion engineering and oxygen control identified to improve AM machinability.

## GRAPHICAL ABSTRACT

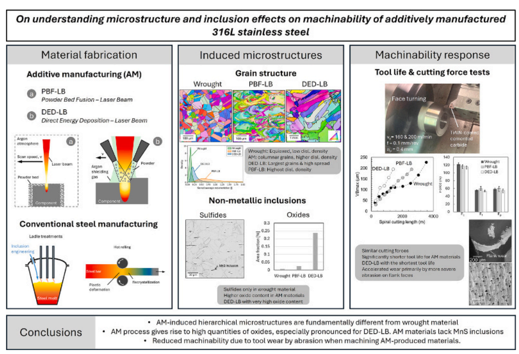


## ARTICLE INFO

*Keywords:*
Machinability
Tool wear
Additive manufacturing
Stainless steel

## ABSTRACT

Additive manufacturing (AM) enables near-net shape parts with complex geometries, but precision components require machining to meet surface requirements. This study links fabrication-induced microstructures to turning machinability of 316L stainless steel produced by laser powder bed fusion (PBF-LB) and directed energy deposition (DED-LB). Unlike previous studies focusing primarily on grain structure and anisotropy, this work identifies non-metallic inclusions as a governing microstructural factor affecting tool wear during machining of AM 316L. Compared with wrought material, AM materials exhibited columnar grains, higher crystallographic misorientation, and a hardness increase of 100% and 45% for PBF-LB and DED-LB material respectively. In addition, higher densities of oxide inclusions were found in the AM variants, whereas wrought material additionally contained sulfides. Although initial cutting forces differed by less than 10%, tool life tests revealed that additively manufactured materials showed consistently faster flank wear development than the wrought material, resulting in earlier attainment of the wear criterion and tool-life reductions of up to ~57%. Non-metallic inclusions were identified as a major factor governing wear progression, suggesting that limiting oxygen uptake and tailoring inclusions could improve machinability.

* Corresponding author.
*E-mail address:* hoierp@chalmers.se (P. Hoier).

https://doi.org/10.1016/j.jmapro.2026.08.017
Received 19 February 2026; Received in revised form 1 July 2026; Accepted 7 August 2026
Available online 25 August 2026

## 1. Introduction

In recent years, additive manufacturing (AM) has developed significantly, with processes such as wire arc additive manufacturing (WAAM) [1,2], directed energy deposition (DED) [3], and powder bed fusion (PBF) using a laser [4,5] or electron beam [6] becoming increasingly established for producing metallic parts. Unlike subtractive machining operations such as turning and milling, which generate the final geometry by removing material from bulk stock, these AM processes fabricate parts by the selective addition of material in successive layers [7]. Optimized AM processes enable the fabrication of nearly fully dense, defect-free, parts from materials including stainless steels, aluminum, titanium, and nickel-based superalloys. The increasing range of available AM materials, together with advantages such as shorter lead times for introducing new materials and part variants into production, material waste reduction and the ability to realize complex geometries, has driven adoption of AM in industries such as automotive, aerospace, and medical [8]. Within this context, additively manufactured 316L stainless steel is of particular interest for corrosion-resistant parts with complex internal features – including compact heat exchangers, manifolds, fluid devices and near-net-shape structural parts. PBF-LB is typically employed for small- to medium-sized parts, whereas DED-LB is used for larger near-net-shape parts and for repair, e.g. cladding of remanufactured parts.

Despite these advances, as-built AM parts rarely satisfy the full set of design and quality requirements – encompassing form, accuracy, surface integrity, and bulk material properties – and therefore require subsequent post-processing. In many cases, additional processing steps such as heat treatment, hot isostatic pressing (HIP), shot peening [9], and laser shock peening [10] are applied to reduce internal defects and residual stresses [8]. Moreover, layer-wise fabrication commonly leads to surface irregularities such as the staircase effect [11] and partially melted or sintered powder particles adhering to the surface, so the as-built surfaces are generally inadequate for functional features such as sealing faces, threaded and precision bores, bearing seats and mating surfaces. These features must therefore be machined to meet the requirements. The amount of stock to be removed after printing depends on the AM technology, process parameters, feedstock material properties, and part design. Post-processing operations may include machining with geometrically defined cutting edges (e.g. turning, milling, drilling), machining with geometrically undefined cutting edges (e.g. grinding [12]), as well as chemical mechanical polishing [13], and non-mechanical finishing methods such as electropolishing [14]. Consequently, an understanding of the machinability of AM 316L is essential for the industrial implementation of PBF-LB and DED-LB processes in production chains.

According to Liao et al. [15] machinability is a generalized measure of how a workpiece material responds to mechanical cutting assessed through cutting forces, tool life, chip formation, or surface integrity. Among these indicators, tool life is the most widely used criterion for machinability evaluation both in academia and industry. Cutting tool life is a function of process conditions (e.g. cutting parameters, cooling/lubrication and machine tool), the properties of the cutting tool (e.g. coating and substrate materials, micro and macro geometry), and the intrinsic properties of the workpiece material. Among the published research on machinability of AM 316L, only few studies address cutting tool wear in detail.

For example, Guo et al. [16] linked machinability to microstructural anisotropy and hardness differences induced by changing build direction. Depending on cutting conditions, about 33–46% higher cutting forces and 6–16% higher tool wear were reported during dry milling when deposited layers are parallel to the machined surface as compared with machining surface orientated perpendicular to the build direction. Kitay and Kaynak [17] examined the effect of the cutting tool geometry on cutting forces, tool wear, chip morphology and surface integrity in turning of PBF-LB/316L. Although no quantitative values were reported, the study indicates that AM material induces greater tool wear than wrought 316L, attributed to higher anisotropy resulting in increased abrasiveness. In addition, the AM material exhibited a thicker machining-affected, particularly at negative tool rake angles. Li et al. [18] investigated tool wear when milling 316L produced by DED-LB using different scanning strategies. Compared to cast 316L, an increase in flank wear land width between 35% and 133% was reported for the same cutting distance when machining the AM variant. This greater flank wear was attributed to higher cutting forces and temperatures encountered by the tool during machining. The flank wear variability of the AM-produced 316L was linked to the laser scanning strategies inducing differences in crystallographic anisotropy, dislocation density, and defect population, all of which affecting forces, temperatures, and hence tool wear development during cutting.

Across these studies, tool wear during machining of AM 316L is consistently attributed to AM-specific microstructural features, including anisotropy and elevated dislocation density. However, the role of non-metallic inclusions in AM 316L remains comparatively unexplored despite evidence that AM processes generate distinct inclusion characteristics. Several studies on AM-processes report noteworthy differences in oxide content, chemistry, and morphology compared to conventionally produced material. For example, Deng et al. [19] report 4–6 higher oxygen levels in PBF-LB processed 316 L as compared with cast, wrought, or welded 316L. Similarly, Eo et al. [20] observed significantly higher oxygen content (300–1000 ppm) in DED-LB processed 316L compared with typical levels below 100 ppm in conventional material. In addition, they report differences in inclusion chemistry, mean diameters, and number density.

Regarding conventionally-produced steels, it has long been established that the characteristics of non-metallic inclusions have a significant impact on machinability, particularly in terms of tool life and chip formation [21,22].

In conventional steelmaking, machinability improvements are often achieved by inclusion engineering, i.e. the controlled formation, composition and distribution of non-metallic inclusions [23]. The effect of inclusions on machining in conventional 316L steel in particular has been investigated by Bletton et al. [24], Hoier et al. [25], and Du et al. [26] – all of whom highlight that inclusion composition and properties can strongly affect tool wear due to changes in the tribological conditions in the cutting zone.

Given the fact that inclusion-characteristics in conventional metallic materials have long been known to be of key importance for machinability, it is surprising that this microstructural feature is often overlooked in machinability research of AM materials.

Although previous studies have consistently reported accelerated tool wear during machining of additively manufactured steel, these differences have primarily been attributed to grain morphology, crystallographic texture, hardness, or dislocation density. Comparably little attention has been paid to the influence of non-metallic inclusions, despite their well-established role in governing machinability in conventionally produced steels. Consequently, the contribution of AM-induced inclusion characteristics remains insufficiently understood.

To address this research gap, the present study investigates how AM-specific inclusion characteristics influence tool wear evolution and tool life during turning of 316L stainless steel produced by PBF-LB and DED-LB. By directly comparing these materials with wrought 316L under controlled machining conditions, the work provides a process-structure-performance link that is relevant to industrial post-processing of AM components. The findings aim to support improving machining strategy selection and highlight inclusion control during AM processing as a potential route for enhanced tool life and reduced machining costs in an industrial scenario.

## 2. Experimental

### 2.1. Workpiece materials

The workpieces investigated in this study were cylindrical hollow bars made of 316L austenitic stainless steel. Details regarding the scan strategy employed for the AM workpieces can be seen in Fig. 1 and are summarized below:

- AM material fabricated by PBF-LB, produced as hollow cylinders (100 mm outer diameter, 50 mm inner diameter, 60 mm length) using an EOS M290 machine equipped with a 400 W fiber laser with a spot size of 100 μm. The parts were built using optimized infill and contour parameters with a contour thickness of 70 μm. The infill was printed with a laser power of 214 W, a scan speed of 928 mm/s, a layer thickness of 40 μm, and a hatch distance of 100 μm. A stripe scan strategy was employed with a stripe width of 12 mm and a stripe overlap of 90 μm. A scan rotation of 67° was used between consecutive layers. The contours were printed with a laser power of 136 W and a scan speed of 447 mm/s. No post-processing heat treatment was performed. The resulting density was approximately 99.98% (quantitative image analysis on polished cross-sections).
- AM material fabricated by DED-LB, produced as hollow cylinders (100 mm outer diameter, 50 mm inner diameter, 60 mm length) using a 1500 W laser. The secondary and central shielding gas flow rates were 10 l/min and 6 l/min, respectively. The nozzle-workpiece distance was 13 mm and the laser spot diameter 2.25 mm. The deposition speed was 2000 mm/min, and the vertical and lateral increments were 0.6 mm and 1.5 mm, respectively. No post-processing heat treatment was performed. The resulting density was approximately 99.89%.
- Conventional wrought material (hot-rolled), supplied in solution annealed and quenched condition, and subsequently machined into hollow cylinders (95 mm outer diameter, 50 mm inner diameter, 60 mm length).

To eliminate the effects of as-built surface topography and microstructural gradients in the AM materials, the outer surface layers of the AM workpieces were machined away prior to the machinability tests. The chemical composition of all investigated workpieces was determined by an ISO 17025 accredited laboratory [27] using standardized ASTM methods as detailed in Table 1.

### 2.2. Machining tests

Face turning tests were performed on an EMCO TURN 365 CNC lathe. All workpieces were machined under two cutting conditions (Table 2) using PVD-coated (TiAlN) cemented carbide inserts of type TCMT 16 T304-MF 1125 (see Fig. 1d). The inserts were mounted on a CoroTurn 107 STGCR 2525 M 16 tool holder, resulting in $\psi_r = -1^\circ$ tool lead angle, $\lambda_s = 0^\circ$ tool cutting edge inclination angle, and $\alpha_n = 7^\circ$ tool normal clearance angle. The machining parameters were selected to represent typical finishing conditions for 316L stainless steel. The feed rate and depth of cut constant were kept constant to isolate material effects. The cutting speed was varied at two levels due to its dominant effect on cutting zone temperature, tool wear mechanisms, and tool life. Cutting forces were measured using a piezoelectric three-component force dynamometer (Kistler 9257A), mounted between the lathe turret and tool holder, as shown in Fig. 1c. Fig. 1c also presents the overall experimental configuration, including the dynamometer and the relationship between feed direction and build direction of the workpieces.

The first set of cutting tests was designed to compare tool-wear behavior when machining the workpiece materials concerned. The

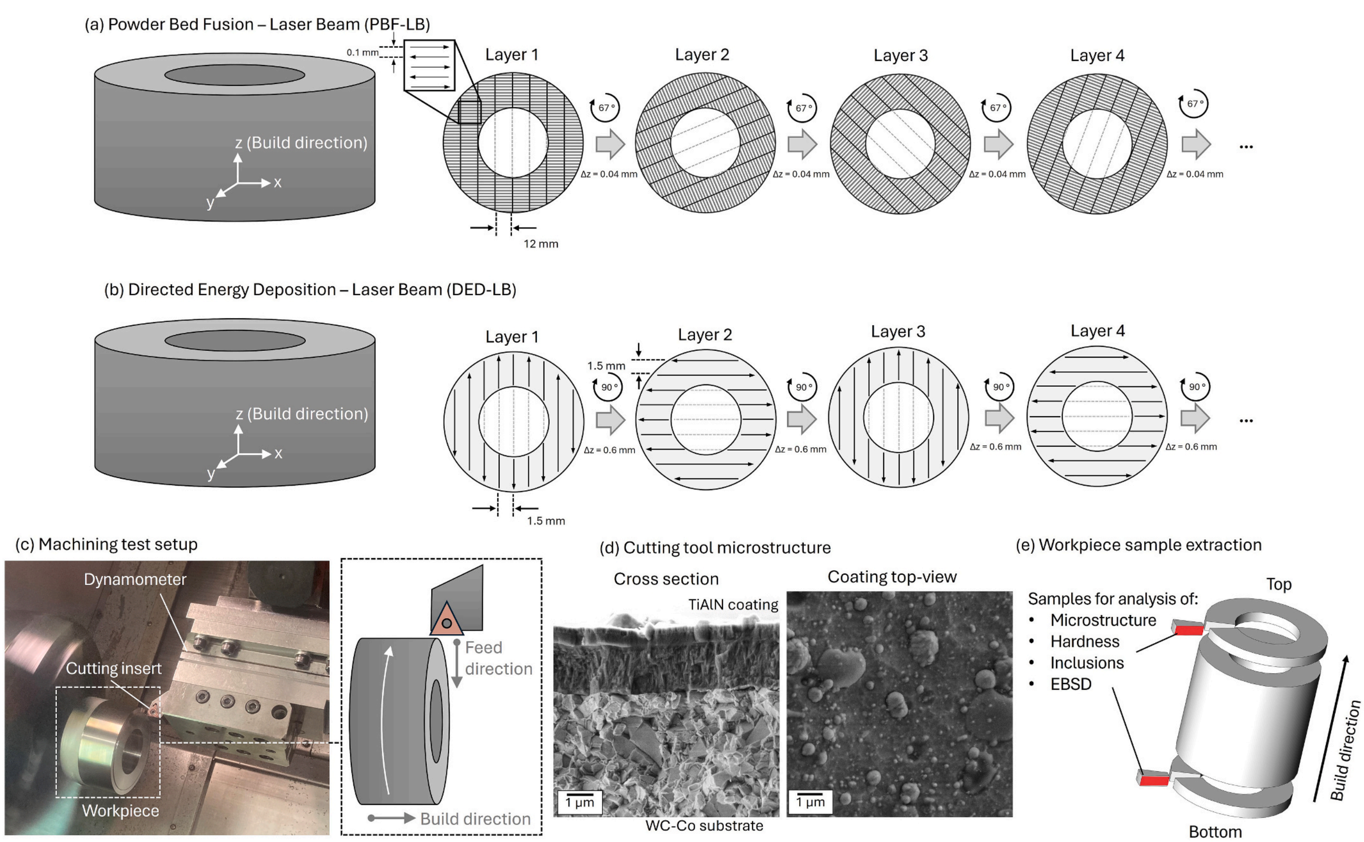


**Fig. 1.** Experimental details of workpiece fabrication via AM (a, b), machining tests with dynamometer and feed/build direction relationship (c), cutting tool microstructure (d), and locations of metallographic sample extraction from workpiece (e).

**Table 1**
Chemical composition of the investigated workpieces (wt%) determined by accredited laboratory using X-ray spectrometry and optical emission spectrometry in accordance with ASTM E572 [28] and ASTM E1086 [29]. Carbon, sulfur, and oxygen were measured by combustion techniques following ASTM E1019 [30].

| Workpiece | C | Si | Mn | P | S | Cr | Ni | Mo |
|---|---|---|---|---|---|---|---|---|
| Wrought | 0.015 | 0.28 | 1.80 | 0.026 | 0.029 | 16.73 | 11.13 | 2.10 |
| PBF-LB | 0.012 | 0.57 | 1.37 | 0.016 | 0.006 | 16.88 | 12.90 | 2.60 |
| DED-LB | 0.008 | 0.75 | 1.57 | 0.012 | 0.006 | 17.04 | 12.43 | 2.58 |

| Workpiece | Cu | Co | V | Al | Ca | B | O | Fe |
|---|---|---|---|---|---|---|---|---|
| Wrought | 0.26 | 0.098 | 0.039 | 0.005 | 0.0028 | 0.0005 | 0.005 | Bal. |
| PBF-LB | 0.039 | 0.050 | 0.022 | 0.008 | <0.0003 | 0.0017 | 0.059 | Bal. |
| DED-LB | 0.057 | 0.029 | 0.022 | 0.005 | 0.0005 | 0.0021 | 0.087 | Bal. |

**Table 2**
Cutting parameters used during face turning of all investigated workpieces.

| | Cutting speed, $v_c$ [m/min] | Feed rate, $f$ [mm/rev] | Depth of cut, $a_p$ [mm] |
|---|---|---|---|
| Condition A | 160 | 0.1 | 0.4 |
| Condition B | 200 | 0.1 | 0.4 |

tests were therefore conducted in intervals. After each cutting interval, the cutting inserts were inspected using a stereo-optical microscope. Tool life was evaluated using the commonly adopted maximum flank wear criterion (VBmax) [31]. End of tool life was defined as a maximum flank wear width of 150 μm for Condition A and 200 μm for Condition B. The tests were stopped when either the corresponding wear criterion or the maximum cutting time of 20 min was reached. Each test was conducted twice to ensure the repeatability of the observed behavior.

In addition to the tool-life tests, a second set of tests was performed to compare the effect of workpiece materials on cutting forces. These tests were conducted with short cutting times chosen such that insignificant tool wear developed. For each workpiece-cutting-condition combination, three tests were conducted, and the results were averaged. Each test was started with a new, unworn insert to isolate the influence of the workpiece material from other process-related effects, such as differences in tool geometry arising from evolving wear.

### 2.3. Characterization of workpieces and tool wear

The microscopic analysis of the workpieces and worn cutting tools was largely carried out using Light Optical Microscopy (LOM) and Scanning Electron Microscopy (SEM). SEM investigations were performed using a LEO 1550 Gemini SEM and FEI/Philips XL-30 SEM, equipped with detectors for Energy-Dispersive X-ray Spectroscopy (EDS) and Electron Backscatter Diffraction (EBSD).

Metallographic samples of the AM 316L workpieces were extracted from the positions indicated in Fig. 1e to assess potential through-build variations. Two samples were extracted from each part. One sample from close to the bottom of the part (early build stage) and one from the top (final build stage). For consistency, specimens from the wrought material were also obtained from two locations within the supplied bar. After mounting in a conductive bakelite hot-mounting resin, the samples were mechanically ground and polished. The polished, unetched samples were then examined using a variety of qualitative and quantitative metallographic methods.

The hardness of workpiece materials was determined using a Vickers hardness indenter with a test force of 5 kgf (HV5). A total of 20 indents, evenly distributed across the surface of each sample, were performed. For the AM materials, samples from both the top and bottom of the workpieces were tested.

The types, quantities and compositions of non-metallic inclusions were investigated for each workpiece material. For this purpose, a combination of LOM and SEM with EDS was used. For each workpiece, the chemical composition of at least 30 inclusions was determined by EDS to identify and classify the inclusion types present. The image-processing software ImageJ was used to determine the amount and size of inclusions visible on micrographs of unetched metallographic samples. Since the inclusions covered a wide size range, the quantification was subdivided into two sets of images. Inclusions with areas between 1 μm$^2$ to 10,000 μm$^2$ were quantified on SEM images using backscatter electron detector at 500× magnification (18 mm$^2$ total investigated area). Larger inclusions (> 10,000 μm$^2$), observed only occasionally, were analyzed on light optical images acquired at 50× magnification (585 mm$^2$ total investigated area).

EBSD measurements were performed using a LEO 1550 Gemini SEM equipped with an HKL Nordlys detector (Oxford Instruments), and large-area EBSD maps were acquired on a Zeiss Gemini 450 SEM equipped with a Symmetry detector (Oxford Instruments). For the DED samples, large-area scans were specifically carried out to obtain representative grain statistics, accounting for their inherently large grain size. Special care was taken during sample preparation, with final polishing performed using a 0.05 μm colloidal silica suspension to obtain deformation-free surfaces. All EBSD maps were acquired at an accelerating voltage of 20 kV with a step size of 2 μm, and the data presented in this study were analyzed using MTEX, an open-source MATLAB toolbox [32].

In addition, a set of polished samples was electrolytically etched using 10% aqueous oxalic acid to reveal and compare the grain and melt-pool structures of the wrought and AM workpieces on a larger scale. The surfaces of the worn cutting tools were examined by SEM and EDS directly after the cutting tests and after the removal of adhered workpiece material by etching in diluted HCl.

## 3. Results

### 3.1. Workpiece microstructures and hardness

The examination revealed homogeneous microstructures within the workpieces, i.e. no qualitative or quantitative differences were observed between specimens extracted from lower and upper build regions (Fig. 1e). Therefore, the results presented in this subsection are reported collectively for each manufacturing route (e.g. PBF-LB) without further subdivision by sample location.

The initial metallographic examination, shown in Fig. 2, highlights the distinctively different microstructures resulting from the three fabrication methods used to produce the 316L workpieces (for sample orientation relative to print direction see Fig. 1). The conventional wrought material (Fig. 2a) contains non-metallic inclusions with a high aspect ratio, with elongation parallel to the rolling direction introduced during the production of this material. In contrast, both the PBF-LB and DED-LB workpieces show microstructural characteristics that are typical for AM-produced material, including clearly visible melt pool boundaries (Fig. 2b, c) and solidification-induced anisotropy in the build-

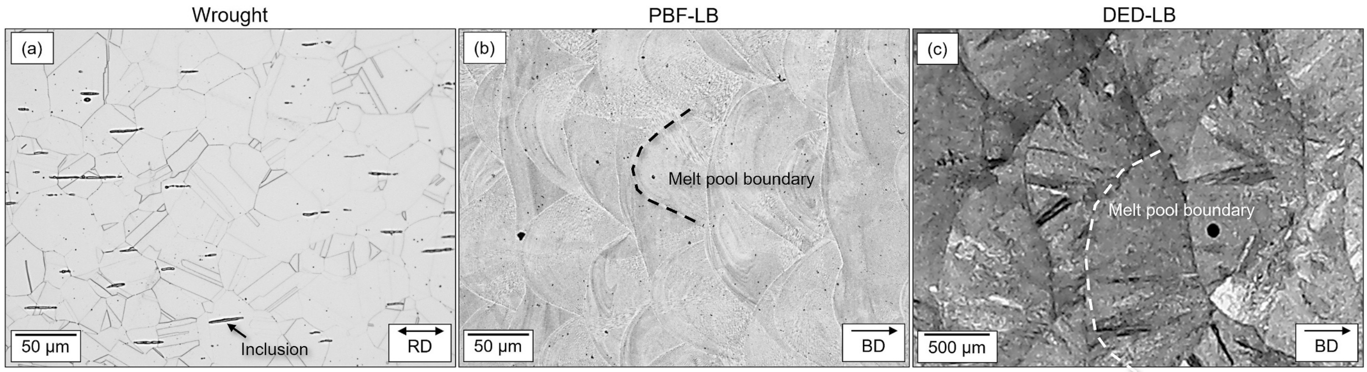


**Fig. 2.** LOM images of etched samples of the investigated 316L workpieces. Rolling direction (RD) and build direction (BD) are indicated with arrows. Note the different length scale in (c).

direction. The micrographs in Fig. 2 also show the significantly different length scales of the microstructural features in the three materials (note the different scale bar for the DED-LB micrographs). The melt pools are significantly larger in the DED-LB material (>1 mm wide) than in the PBF-LB material (about 50–100 μm). No systematic differences between samples taken from the top and bottom of the AM workpieces were observed.

EBSD analysis was used to characterize the microstructure in terms of grain size, crystallographic orientation and texture. The EBSD maps shown in this section show only a representative fraction of the acquired data; in contrast, the grain-diameter and kernel average misorientation (KAM) distributions are based on all EBSD data sets obtained for each material. Fig. 3 shows orientation maps of the three materials along with the corresponding inverse pole figures. The wrought material exhibits a pronounced ⟨111⟩ grain orientation parallel to the rolling direction. The PBF-LB material shows a preferential ⟨011⟩ grain orientation parallel to the build direction, whereas the DED-LB material displays a nearly random texture, with grains exhibiting a weak ⟨011⟩ alignment along the build direction and a slight ⟨111⟩ preference along the normal direction (horizontal plane). The wrought material exhibits equiaxed grains with diameters below 100 μm and contains annealing twins (Fig. 3a). In contrast, both AM materials exhibit elongated, columnar grains predominantly aligned with the build direction. Among the microstructures investigated, the DED-LB material shows the largest grains with the highest aspect ratio. As shown in Fig. 3c, columnar grains reach millimeter-scale lengths, while smaller grains below 100 μm are also present. The PBF-LB material, by comparison, exhibits smaller columnar grains and a narrower grain size distribution (Fig. 3b).

Fig. 4 shows violin plots of the equivalent circular diameter (ECD) of grains derived from the EBSD data (logarithmic y-axis). Since the wrought material exhibits a significant presence of annealing twins, a twinning analysis was performed and twin-related regions with a misorientation angle of ~60° were merged with their parent grains prior to grain-size evaluation. The violin plots reveal clear differences in ECD among the materials. The wrought material exhibits a comparatively narrow ECD distribution with the majority of grains clustered around a limited size range which indicates a comparatively uniform grain size.

The material produced by PBF-LB displays a slightly broader grain size distribution spanning a wider range on the logarithmic scale. Its violin's thickest part is located at a smaller grain size, indicating a smaller median ECD for this material as compared to the wrought counterpart.

The by far widest ECD distribution, spanning across several orders of magnitude, is displayed by the DED-LB material. This indicates a comparably heterogeneous grain size distribution in which very large grains coexist with small grains (see also Fig. 3c). The median and thickest part of the violin occur at the largest ECD of all three materials.

Kernel average misorientation (KAM) analysis was performed for the wrought, PBF-LB and DED-LB samples. KAM quantifies local crystallographic misorientation by calculating the average misorientation angle between each pixel and its neighboring points. It is commonly used as a qualitative indicator of local lattice strains resulting from elevated dislocation densities. Thus, KAM enables a comparative assessment of the stored plastic strain in the investigated workpieces. In this study,

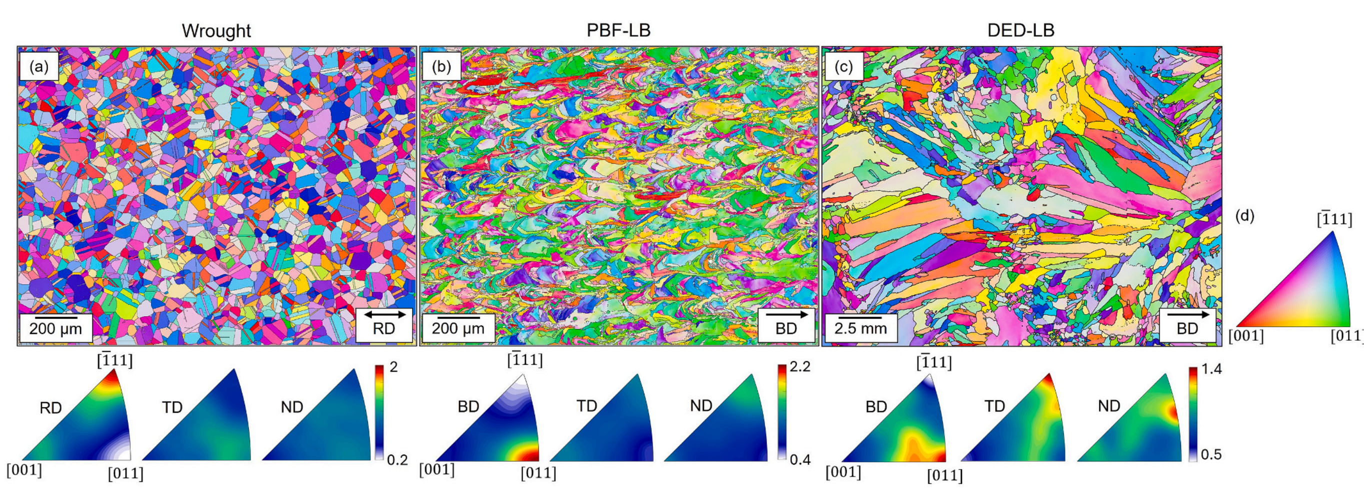


**Fig. 3.** EBSD orientation maps in IPF color-code. Rolling direction (RD) in the wrought workpiece and build direction (BD) in the AM workpieces are indicated with arrows. IPF color code is provided in (d). Note the different length scale in (c).

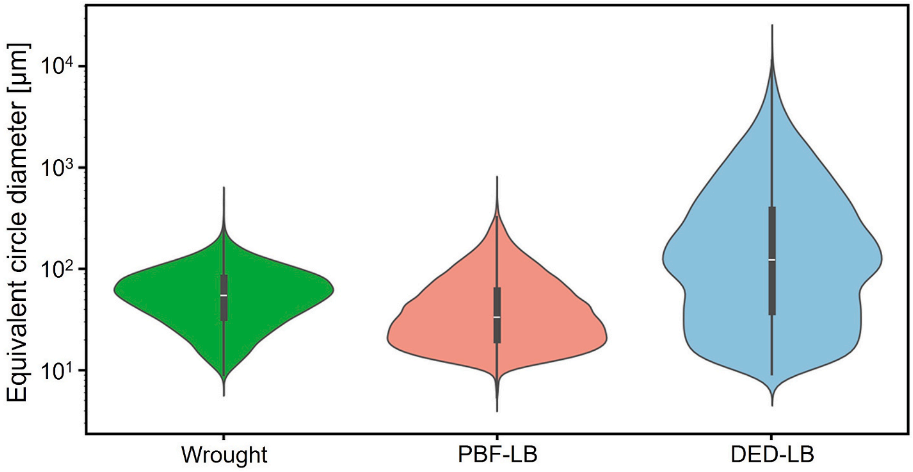


**Fig. 4.** Distribution of grain diameters for the investigated workpieces based on all EBSD data sets.

KAM maps were generated using first-order neighbors with a misorientation threshold of 2.5°. This threshold was selected because KAM values are typically dominated by orientation gradients at sub-grain boundaries; by applying a relatively small cutoff angle ($\delta = 2.5°$), the influence of sub-grain boundaries is effectively minimized. Fig. 5 shows the KAM maps for all three materials. The PBF-LB material exhibits the highest KAM values, reflecting strong orientation variations within grains. The DED-LB material shows intermediate misorientations, whereas the wrought material displays the lowest misorientation.

The corresponding KAM distribution plots derived from the EBSD data sets are shown in Fig. 6 and further highlight the differences between the three materials. The wrought material exhibits the lowest KAM values, predominantly between 0° and 0.25°, with the highest density close to 0.1°. The DED-LB material shows intermediate KAM values spanning a wider range between 0° and 1°, with a peak near 0.25°. In contrast, the PBF-LB sample shows significantly higher misorientations, extending up to about 2°, indicative of considerably higher lattice distortions present in the as-built condition.

Hardness results are summarized in Fig. 7. While the wrought material exhibits an average hardness of 140 HV5, both AM materials exhibit higher hardness of 239 HV5 and 203 HV5 for the PBF-LB and DED-LB material, respectively. No significant difference between samples obtained close to the top and bottom of the AM workpieces were observed.

### 3.2. Non-metallic inclusions

The microstructural examination revealed that all concerned materials contained non-metallic inclusions. These inclusions were distinguished from the steel matrix by utilizing the contrast emerging from

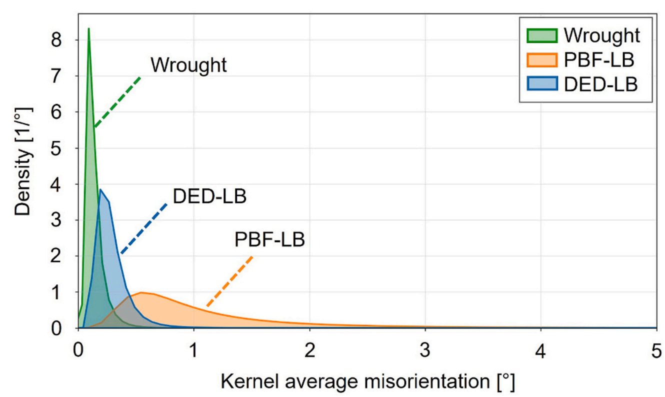


**Fig. 6.** Distribution of Kernel average misorientation measurements in the three workpieces. The data shown is based on all EBSD datasets.

differences in mean atomic number using backscatter electron imaging in the SEM while EDS was employed to verify their composition. Porosities in the AM workpieces yielded no backscattered electrons and therefore appeared black.

EDS analysis of the wrought material showed two main inclusion types: oxides and sulfides (see examples in Fig. 8a and b, respectively). The sulfides were identified as MnS, while the oxide inclusions were rich in Si, Ca and Mn. All 30 oxide inclusions analyzed in this material were found to have the same main elements present, as shown by an example EDS spectrum in Fig. 8c. The presence of Ca is likely related to Ca-treatment during steelmaking, aimed at enhancing machinability by

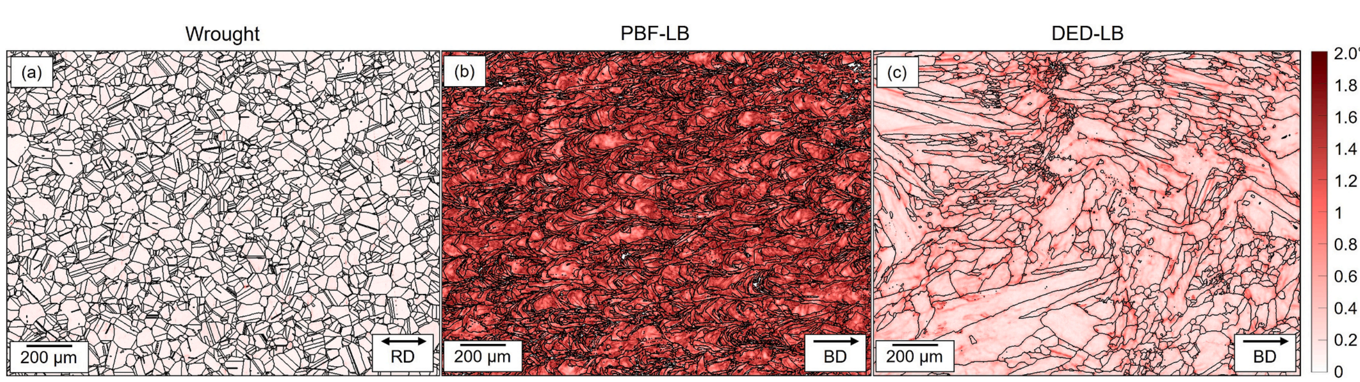


**Fig. 5.** Kernel average misorientation maps (KAM) of the three workpieces.

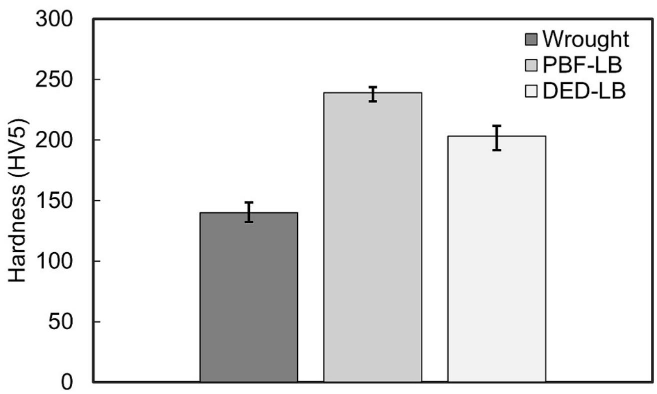


**Fig. 7.** Average Vickers hardness of the workpieces. Error bars represent the spread of measurements.

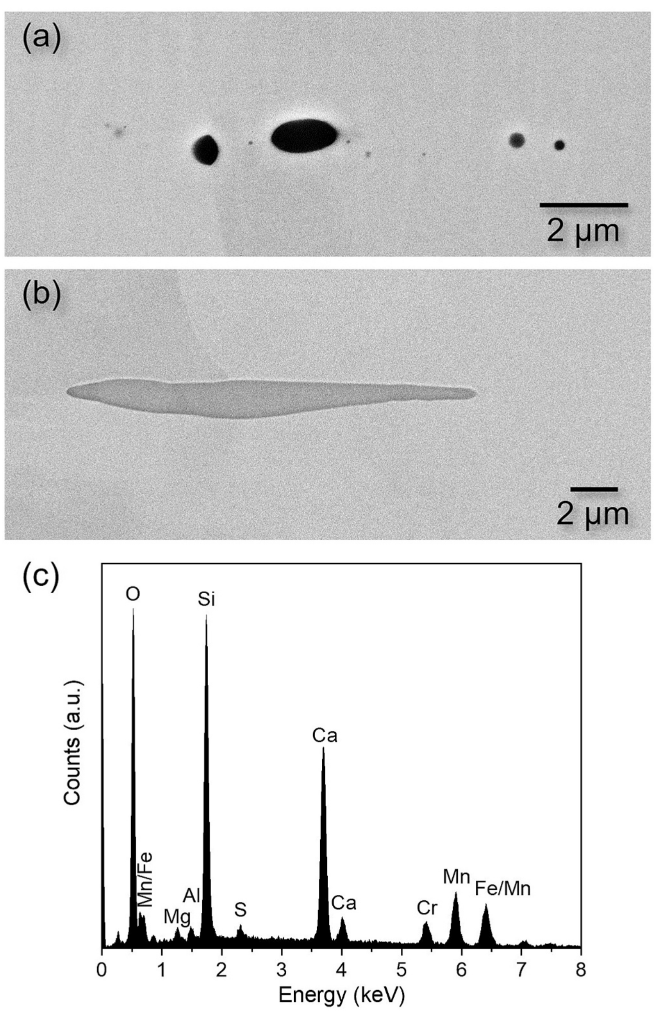


**Fig. 8.** Non-metallic inclusions in the wrought workpiece. SEM micrographs of oxide inclusions (a) and sulfide inclusion (b). EDS spectrum of an oxide inclusion (c).

modifying hard oxide inclusions into softer, more deformable Ca-containing oxides.

For the AM materials, only oxide inclusions were observed; sulfide inclusions, contained in the wrought material, were not present. Furthermore, the morphology of inclusions in the AM workpieces, differed significantly from that in the wrought material. As shown in Fig. 9a-d, most inclusions in the AM materials were in the form of spherical particles, with only a few abnormally large, irregularly-shaped inclusions observed in the DED-LB material.

Comparing the 2 AM workpieces also reveals clear differences in the size distribution of oxide particles. Both materials contain evenly distributed small-scale oxides (Fig. 9a,b). In the PBF-LB workpiece, these nano-scale oxides have diameters below 100 nm (see inlay in Fig. 9a), whereas in the DED-LB material they reach diameters up to 200 nm (Fig. 9b). In addition to this fine dispersion, larger oxide inclusions were also observed occasionally in both AM materials; examples of these coarse particles are shown in Fig. 9c-e.

The oxide inclusions in the AM workpieces varied in composition, containing different fractions of Al, Si, Cr and Mn. Examples are shown in Fig. 10. Notably, none of the investigated inclusions in the AM materials contained significant amounts of Ca, which is a striking contrast to the wrought material, where Ca was consistently present in the oxides.

The quantitative inclusion analysis combined SEM-based measurements (1–10,000 $\mu m^2$) and LOM-based measurements (>10,000 $\mu m^2$), as described in the experimental section, to ensure statistical representation of both fine and occasional large inclusions. Inclusions larger than 1 $\mu m^2$ were quantified in terms of area fraction, number density, and particle size range. The results are summarized in Table 3. For the particle size range covered, the AM materials contained significantly larger fractions of oxide inclusions than the conventional wrought material. Specifically, the oxide area fraction was approximately 3-times higher for the PBF-LB, and about 29-times higher for the DED-LB material. As indicated in Table 3, the AM materials also exhibit higher particle densities (i.e. number of oxides per $mm^2$), which is especially pronounced for the DED-LB material. The size ranges of the observed oxide particles also differ between the materials. The conventional material exhibits a narrower oxide size area range (up to 50 $\mu m^2$), whereas significantly wider ranges were observed for PBF-LB (up to 210 $\mu m^2$) and especially DED-LB (up to 40,810 $\mu m^2$). This large difference in particle size ranges is, however, not reflected in their medians, which are of comparable magnitude for all three materials. This supports the earlier observation that the AM materials, especially the DED-LB, contain a small number of abnormally large oxides leading to a higher overall oxide content compared with the wrought material, where a narrower range of more evenly sized oxides is prevalent. It should be emphasized that smaller oxides with areas below 1 $\mu m^2$ are not accounted for in this quantification. This leads to an underestimation of the oxide content in the PBF-LB and DED-LB workpieces, where very fine oxide particles were observed (see Fig. 9).

MnS particles were only observed in the wrought material (Table 3). In this workpiece, MnS constitutes a major fraction of the non-metallic inclusions, as reflected by the higher area fraction and higher density of the sulfides compared with the oxides.

### 3.3. Tool wear behavior and cutting forces

The average cutting forces measured during turning of the workpieces are summarized in Fig. 11. Within the experimental scatter, no significant differences in forces acting on the tools were observed. Similar values were obtained for all three force components ($F_c$, $F_f$, and $F_p$) under both tested conditions (Fig. 11a,b).

To further assess the machinability of the three materials, the results of the tool-life tests are plotted in Fig. 12. Flank wear was the dominant wear form for all workpieces. However, the rate of flank-wear development differed significantly between the materials. Under both cutting conditions, machining the AM workpieces led to a faster progression of flank wear compared with the conventional wrought material (Fig. 12a, b). SEM images of worn cutting tools are shown in subsection 3.4 As summarized in Table 4, for condition A the tool-life criterion of 150 μm width of flank wear land was reached after about 18.1 min and 13.8 min for the PBF-LB and DED-LB workpieces, respectively, whereas the

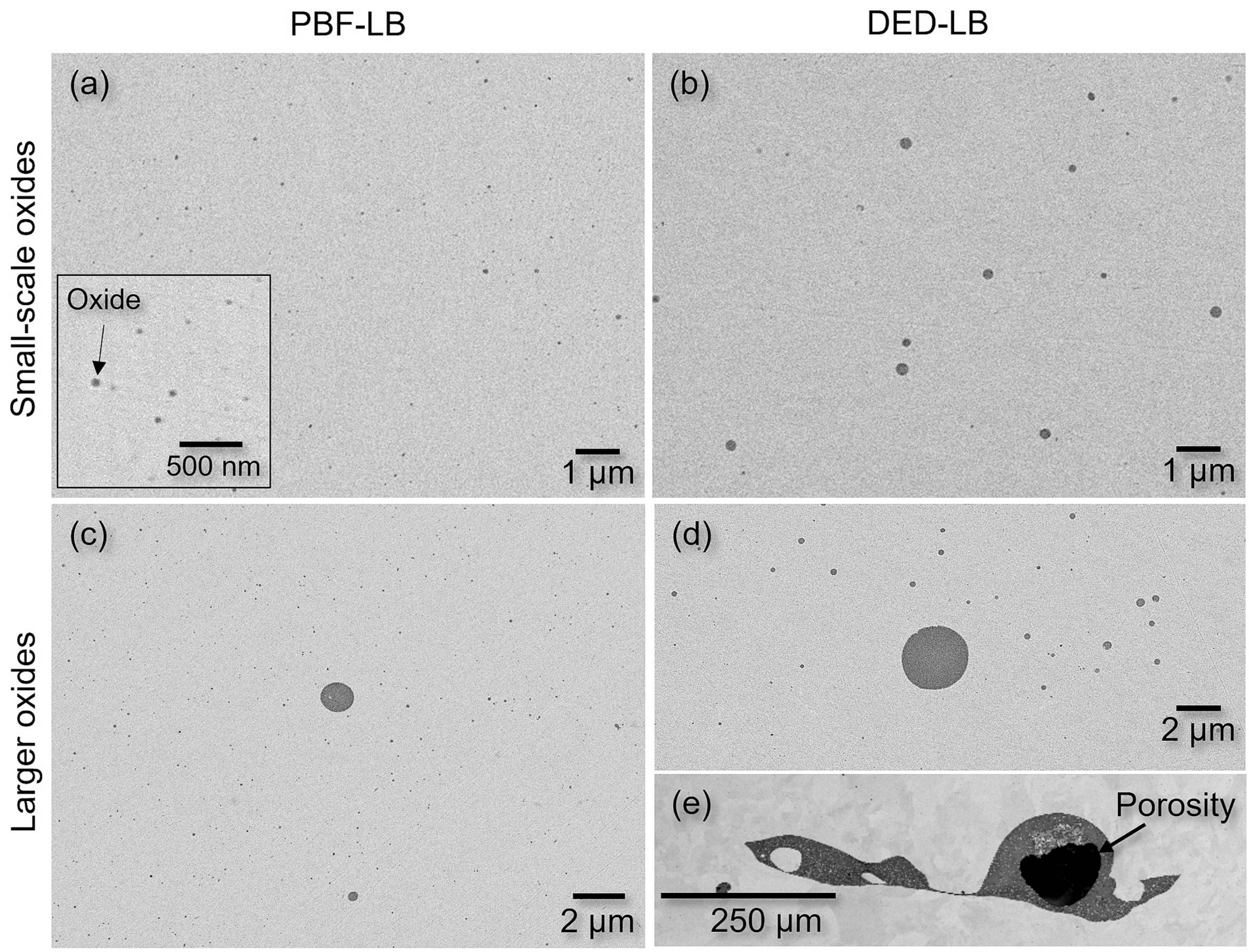


**Fig. 9.** Distribution of oxide inclusions in the AM workpieces (backscatter electron detector images). Higher magnified view of evenly distributed small-scale oxides in PBF-LB (a) and DED-LB (b). Lower magnified view of occasionally occurring larger oxides in PBF-LB (c) and DED-LB (d), (e).

criterion was not reached for the wrought workpiece within the maximum cutting time of 20 min. For the cutting condition B, the tool-life criterion of 200 μm width of flank wear land was reached after around 7.1 min and 13.0 min for the DED-LB and PBF-LB workpieces, respectively, while a cutting time of 16.5 min was achieved for the conventional wrought workpiece (see Table 4). In other words, this corresponds to a reduction in tool life of approximately 21.2% for the PBF-LB and 57.0% for the DED-LB material relative to the wrought material.

### 3.4. Wear characterization

Overviews of the worn cutting edges at the end of tool life are presented in Fig. 13. Most worn areas on the flank and rake faces are covered by adhered workpiece material (appearing with approximately the same grayscale as the tool coating). Only in the close vicinity of the cutting edge, bright areas are visible, corresponding to regions where the WC-Co tool substrate is exposed. The tool used for machining DED-LB material (Fig. 13c) represents an exception: most of the flank-wear land around the tool nose is free of adhered workpiece material. Instead, it can be observed that the tool coating is largely removed, and the WC-Co substrate is exposed.

To obtain a clearer view of the overall geometry of the worn cutting tools and the underlying microscopic wear patterns, the adhered material was removed by etching. Adhesion-free images of the etched cutting edges are shown in Fig. 14. The bright-contrast areas mark zones where the tool coating has been worn away and the WC-Co substrate is exposed. Locally, chipping was observed on some cutting tools, the characteristic wear morphology is exemplified in Fig. 14g. A comparison with the unworn tool surface (Fig. 1d) reveals that the coating is missing. The underlying substrate's wear topography is characterized by smoothly worn WC grains in areas where flank wear developed progressively. In contrast, zones subjected to chipping exhibit a fracture surface-like appearance due to breaking-off of the tool coating. All cutting tools exhibited minor notch wear at the depth-of-cut line on the major cutting edges. The identification of notch wear was based on morphological evidence after removal of adhered workpiece material However, no significant differences in notch-wear behavior are observed between tools used for machining different workpiece materials. The adhesion-free tool surfaces also reveal that chipping of both the coating and the substrate is an active wear mechanism during machining of all three workpieces.

Higher-magnification views of the worn tool surfaces are provided in Fig. 15. The progressive wear of the coating, with ridge-like features oriented parallel to the sliding direction of the chip, can be seen in Fig. 15a. In addition, regions where the WC-Co substrate is exposed due to localized chipping of the coating together with microcrack formation in the coating (see inlay), can be observed. Fig. 15b exemplifies chipping

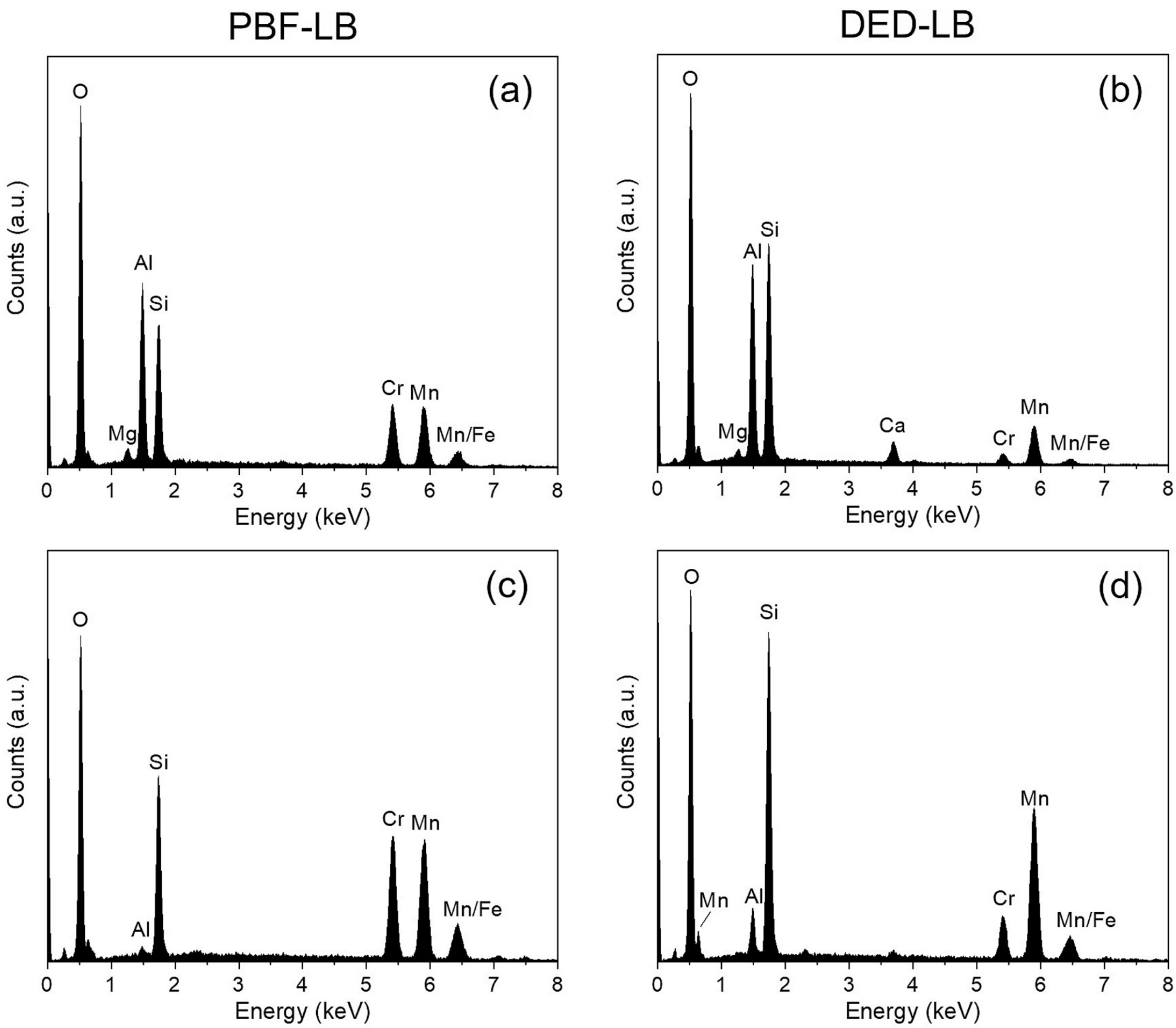


**Fig. 10.** EDS spectra of the types of larger non-metallic inclusions found in the AM materials. Al-Si-Mn-Cr-rich oxide in PBF-LB (a); Al-Si-Mn-Cr-rich oxide in DED-LB (b); Al-Si-Mn-Cr-rich oxide in PBF-LB (c); Si-Mn-Al-rich oxide in DED-LB.

**Table 3**
Summary of quantification of non-metallic inclusions present in the workpieces.

| | | Wrought | PBF-LB | DED-LB |
|---|---|---|---|---|
| Oxides | Area fraction [%] | 0.0083 | 0.027 | 0.24 |
| $> 1\ \mu m^2$ | Density [1/mm$^2$] | 28.09 | 31.20 | 47.20 |
| | Area range [μm$^2$] | 1–50.74 | 1–210.45 | 1–40,810.65 |
| | Median of area [μm$^2$] | 1.93 | 2.69 | 2.12 |
| Sulfides | Area fraction [%] | 0.14 | – | – |
| $> 1\ \mu m^2$ | Density [1/mm$^2$] | 184.90 | – | – |
| | Area range [μm$^2$] | 1–178.32 | – | – |
| | Median of area [μm$^2$] | 3.08 | – | – |

of tool material (substrate and coating) from the cutting edge at the transition from rake to flank face. Examples of the topography of worn WC grains on the flank and rake faces are shown in Fig. 15c and d, respectively. Worn WC grains generally exhibit either a smooth appearance (see upper part of micrograph in Fig. 15c) or a rough surface topography associated with a fine tribo-layer with nanometer-scale features on the majority of WC grains (see lower part of Fig. 15c and Fig. 15d). On the rake faces of all tested tools, worn WC grains are predominantly covered by such nanometer-scale tribo-films (Fig. 15d). In contrast, all investigated flank-wear lands feature a mixture of smooth WC grain surfaces and WC grains partially or fully covered by thin tribo-layers (Fig. 15c). No clear trend in these wear patterns could be identified between tools used for machining the different workpieces: rake faces consistently show WC grains with tribo-layers, whereas flank faces exhibit a mix of smooth, adhesion-free WC grain surfaces and grains covered by thin tribo-films.

## 4. Discussion

This study investigates how workpiece microstructure influences tool wear in turning of 316L austenitic stainless steel produced by AM. Under identical cutting conditions, the turning tests yielded markedly different tool-wear behaviors even though the measured cutting forces were similar.

The present observations are generally consistent with previous studies on the machinability of additively manufactured 316L stainless steel, which have likewise reported accelerated tool wear and reduced tool life compared with conventionally produced material [16–18]. While several previous studies also associated the increased wear with elevated cutting forces [16,18], the present work showed comparable cutting force levels for all investigated materials despite pronounced differences in tool wear. The following sections discuss these observations in relation to the microstructural characteristics of the investigated workpiece materials and their influence on the machining process.

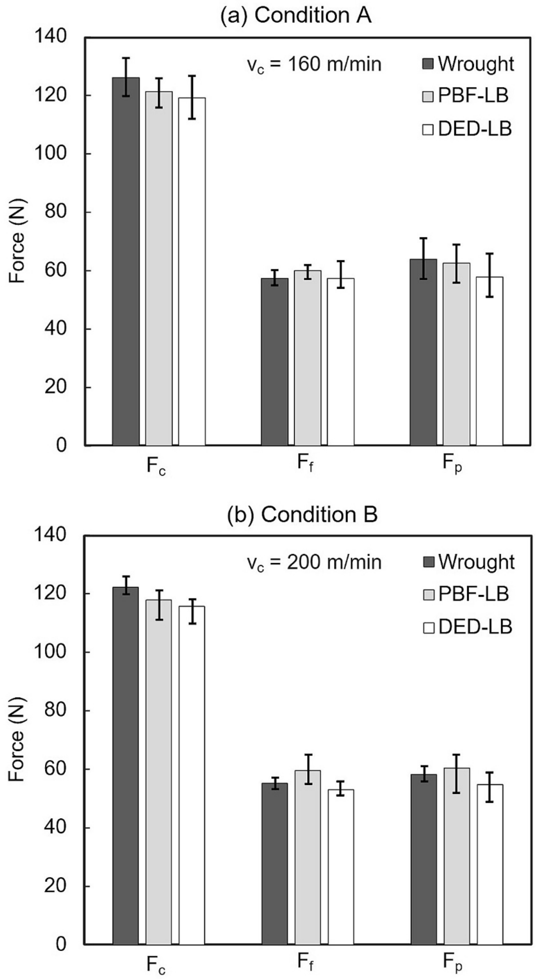


**Fig. 11.** Average cutting forces during face turning of the three workpieces for cutting condition A (a) and B (b). Main Cutting force ($F_c$), feed force ($F_f$), and passive force ($F_p$) were measured when cutting with fresh, unworn tools.

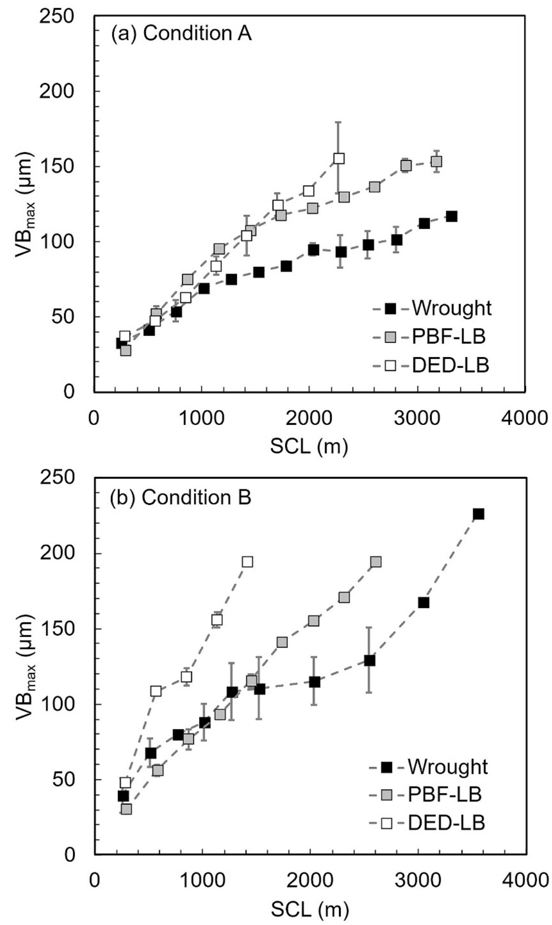


**Fig. 12.** Development of maximum width of flank wear land ($VB_{max}$) as function of spiral cutting length (SCL) for the three workpiece variants and the two cutting conditions using cutting speeds of 160 m/min (a) and 200 m/min (b).

**Table 4**
Tool-life results for turning tests conducted on the three workpieces.

| Cutting condition | Workpiece | Tool life – SCL (m) | Tool life – Cutting time (min) |
|---|---|---|---|
| A | Wrought | >3310 | >20.0 |
| | PBF-LB | 2890 | 18.1 |
| | DED-LB | 2200 | 13.8 |
| B | Wrought | 3300 | 16.5 |
| | PBF-LB | 2600 | 13.0 |
| | DED-LB | 1420 | 7.1 |

### *4.1. Microstructural characteristics of workpiece materials*

A metallic material's microstructure, its physical and chemical properties, and the resulting thermo-mechanical and tribological loads on the cutting tool surface during machining are known to play a key role in tool wear [15]. In the present study, the microstructural examination of the three investigated 316L materials revealed clear differences in texture, grain size distribution, crystallographic misorientation (KAM), and the type and quantity of non-metallic inclusions.

The wrought material's uniform, equiaxed grain structure without significant crystallographic misorientation (reflecting a reduced dislocation density) is characteristic of hot-rolled and solution-annealed austenitic stainless steel. Hot rolling with controlled deformation at elevated temperature promotes dynamic recrystallization and the formation of fine, equiaxed grains [33]. Another consequence of the hot rolling is the development of a crystallographic texture with a preferential ⟨111⟩ grain orientation parallel to the rolling direction (Fig. 3). During hot rolling, non-metallic inclusions are broken up, partly deformed and re-distributed in the steel [33], which explains the relatively even spatial distribution and elongated morphology of the inclusions observed in the wrought material (Fig. 2a and Fig. 8).

In contrast, the PBF-LB and DED-LB workpieces exhibit AM-characteristic microstructures with columnar, elongated grains with high aspect ratios and pronounced crystallographic misorientation. The morphology of the solidification structure in AM is largely determined by local temperature gradients and crystal growth rates [34]. Localized melting and rapid solidification with directional heat conduction promotes grain growth aligned with the build direction, where the maximum heat flow occurs. AM process parameters employed in this study resulted in columnar grain growth for both PBF-LB and DED-LB (see Fig. 3). The markedly different grain size (see Fig. 4) can be attributed to differences in cooling rate: during DED-LB, cooling rates are typically several orders of magnitude lower than in PBF-LB [35,36], which explains for the substantially coarser solidification structure in the DED-LB material.

The presence of crystallographic misorientation in AM-produced 316L materials is a commonly reported feature and is associated with high dislocation densities generated during printing [37]. Dislocation generation and evolution are controlled by rapid cooling, high thermal gradients and repeated thermal cycling during the layer-by-layer build.

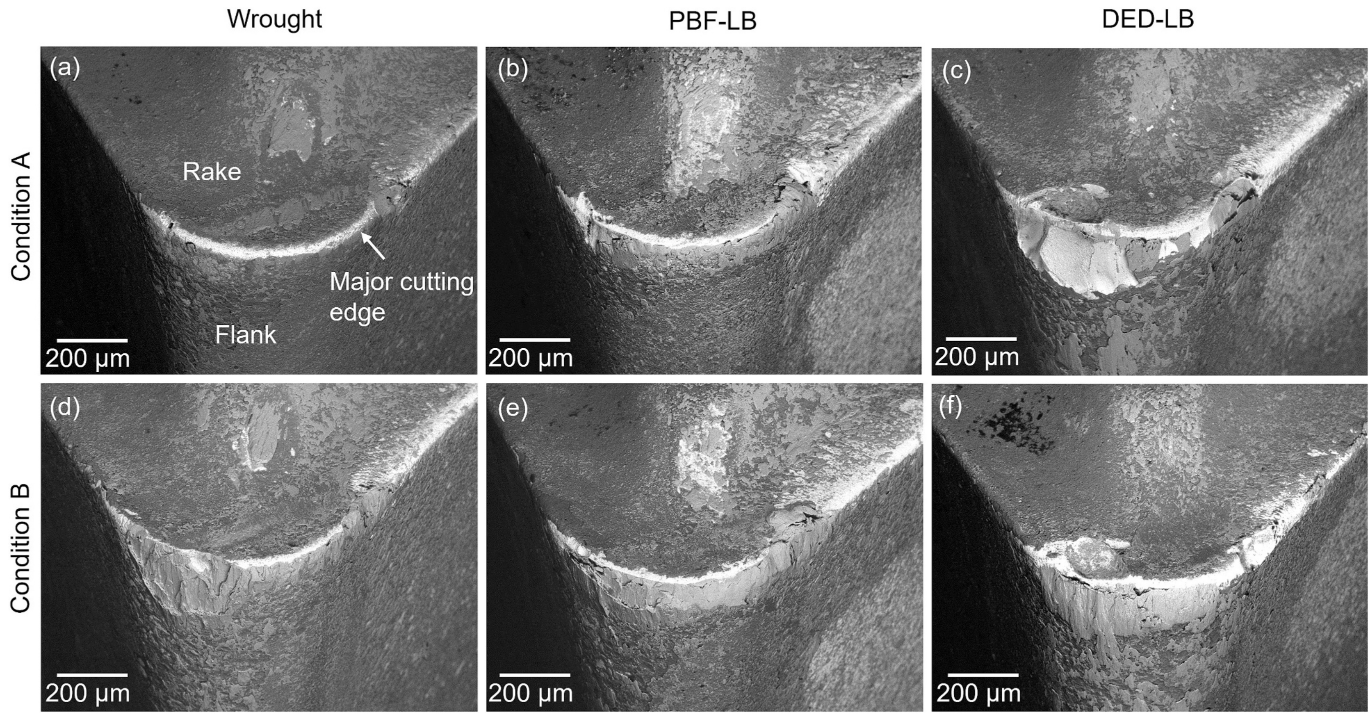


**Fig. 13.** Overview SEM images (Backscattered electron detector) of cutting edges after the tool-life tests for condition A (a)-(c) and B (d)-(f).

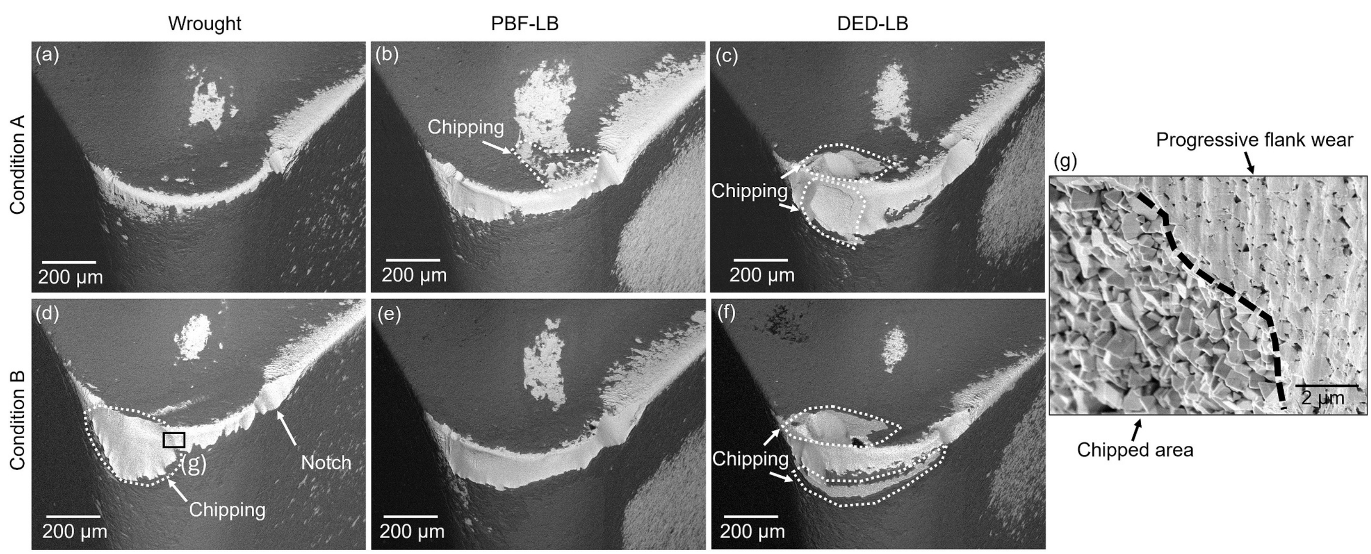


**Fig. 14.** Overview SEM images (backscatter electron detector) of worn cutting edges after removal of adhered 316L workpiece material. Shown are cutting edges after the tool-life tests under condition A (a)-(c) and B (d)-(f). A higher magnified view of the transition from chipped area to progressively worn area is provided in (g).

Gao et al. [38] reported a sharp increase in dislocation density linked to the eutectic solidification reaction, where volumetric mismatches and differences in thermal expansion and mechanical properties between ferrite and austenite produce significant thermal stresses. Subsequent thermal cycles promote dislocation rearrangement due to annealing and dynamic recovery [38]. In the present study, significant crystallographic misorientation was observed for both AM materials, with the PBF-LB exhibiting the highest KAM values (Fig. 5 and Fig. 6), indicative of higher dislocation densities. This can be attributed to higher temperature gradients and cooling rates in PBF-LB, which promote higher thermal stresses, and consequently, greater dislocation generation [38]. The DED-LB material shows relatively lower misorientations, in line with less severe thermal gradients and slower cooling rates during deposition, and thus a lower tendency for dislocation accumulation than in PBF-LB [38].

Compared to the wrought material, the AM workpieces also differ in terms of texture. The PBF-LB workpiece shows a preferential ⟨011⟩ orientation parallel to the build direction, which is in agreement with observations by Wang et al. [39] and Leicht et al. [40]. Similarly, the absence of clear texture for DED-LB processed 316L was also reported by Lee et al. [41].

These microstructural differences are directly reflected in the measured hardness values, which are highest for PBF-LB, intermediate for DED-LB, and lowest for the wrought material (Fig. 7). Strengthening

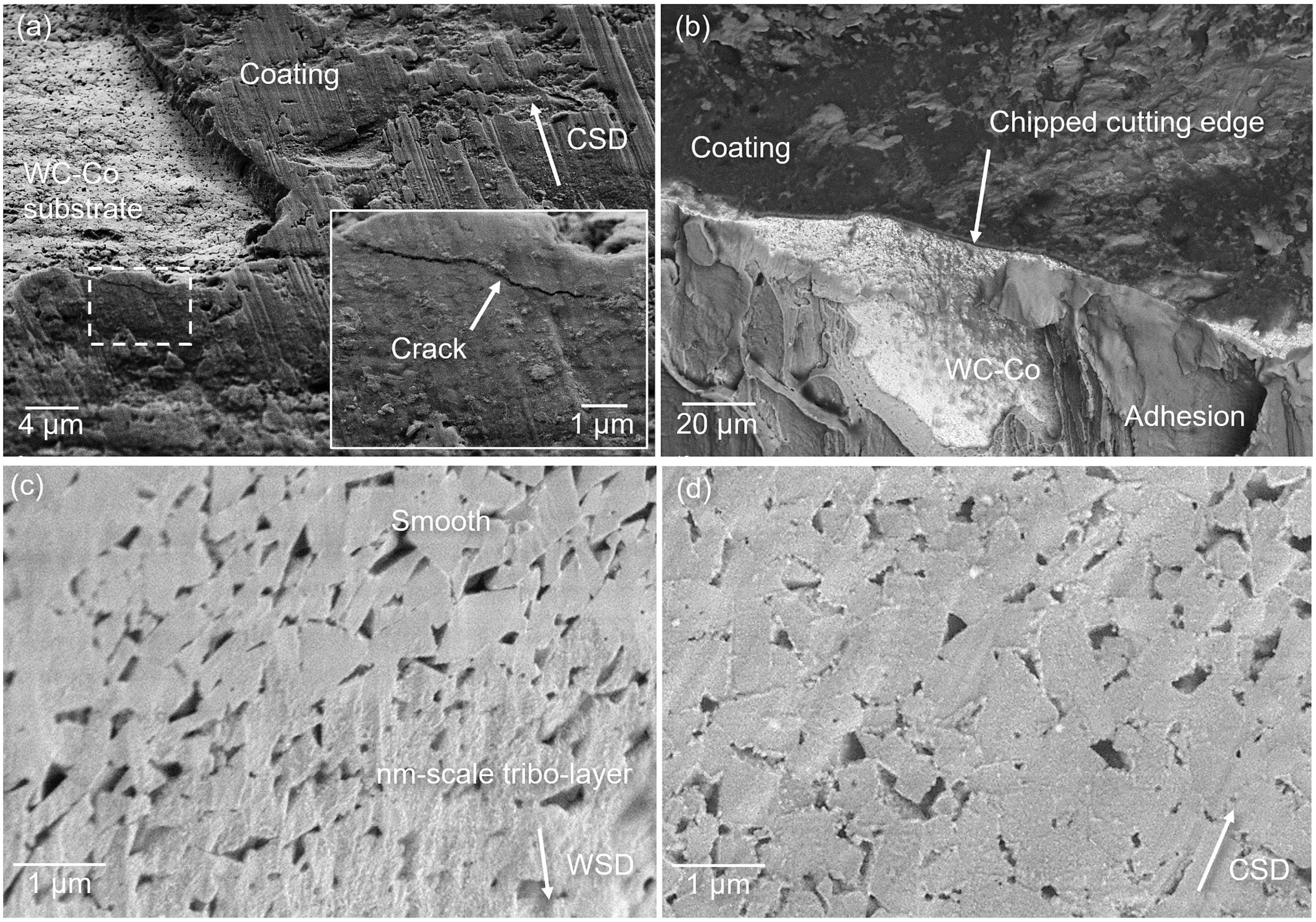


**Fig. 15.** SEM micrographs exemplifying wear patterns on the tools. Cracking and chipping of tool coating on rake face after machining DED-LB workpiece under condition B (a); chipped cutting edge after machining wrought workpiece under condition B (b); WC grain topographies on flank face after machining wrought workpiece under condition A (c); WC grain topography on rake face after machining DED-LB workpiece under condition A (d). Chip and workpiece sliding directions (CSD and WSD) are indicated by arrows.

mechanisms in PBF-LB/316L were investigated by Yan et al. [42], who attributed the high strength in the as-built condition to a combination of Orowan strengthening (due to finely-dispersed oxides) and dislocation strengthening. The reported hardness values of as-built material was around 250 HV, with subsequent heat treatment at 1200 °C leading to a gradual hardness decrease due to dislocation elimination (recrystallization), grain growth, and oxide growth (loss of Orowan strengthening) [42].

In the present study, where no heat treatments were applied, the roughly 15% lower hardness of the DED-LB sample relative to PBF-LB can be explained by both its lower dislocation density (indicated by the lower KAM values in Fig. 5) and its coarser oxide particles (Fig. 9). Consequently, both dislocation strengthening and Orowan strengthening by nanometer-scale oxides are expected to be less pronounced in the DED-LB material. In addition, the larger grain size of the DED-LB material suggests a lower contribution from grain-size strengthening, which may also contribute to its lower hardness compared with PBF-LB.

For the wrought material, by contrast, no significant dislocation density (see low KAM in Fig. 5) and no nanometer-scale oxides comparable to those in the AM materials (Fig. 9) were identified (Fig. 8). All oxide inclusions were in the μm-size range, which is typical for conventionally-processed steels [43]. The absence of both dislocation strengthening and nm-scale Orowan strengthening explains for the about 41% lower hardness of the wrought material relative to PBF-LB.

In summary, the AM 316L workpieces differ fundamentally from their wrought counterpart due to their distinct processing histories. AM-processed stainless steel develops complex hierarchical microstructures which are fundamentally different from wrought material in terms of inclusion size distribution, inclusion chemistry, grain size and morphology, and dislocation density. These differences are interrelated and are expected to affect machinability through distinct, interrelated mechanisms; their individual contributions cannot be readily isolated. In the following subsections, the combined effects of these microstructural features on thermo-mechanical loads and tool wear are discussed in greater detail.

### *4.2. Thermo-mechanical loads on cutting tools*

Cutting forces reflect the workpiece's resistance to deformation and chip formation under the severe thermo-mechanical conditions prevailing in the cutting zone (high strains, strain rates and temperatures) in a better way than conventional mechanical tests (e.g. hardness testing). As highlighted by Malakizadi et al. [44], the material response obtained from conventional mechanical testing can differ significantly from the material behavior during machining. Experimentally complex specialized dynamic material testing systems like the Split-Hopkinson pressure bar can be used to test material behavior under conditions relevant for metal cutting [45]. In the present study, in-process force monitoring revealed that the three workpiece materials generated similar cutting forces (for initially sharp tools), suggesting similar mechanical loads on the tool despite the varying microstructures and hardness of the workpieces. A possible explanation for this behavior is the large strains, high strain rates, and elevated temperatures in the primary shear zone. Due to such conditions, it is the flow stress rather than quasi-static hardness or yield strength that governs material deformation and separation. Differences in the initial microstructure may therefore diminish due to the combined effects of strain hardening, strain rate sensitivity, and thermal softening, leading to similar effective flow stresses and consequently, similar cutting forces. The markedly different tool-wear rates observed are therefore not expected to arise from differences in the cutting forces acting initially on sharp, unworn tools.

Thermo-mechanical loads in the cutting zone arise from the coupling of the mechanics and heat transfer of the machining process. These loads are governed by: (i) process geometry and kinematics (e.g., cutting tool geometry, tool cutting edge engagement, depth of cut cutting speed, feed); (ii) physical/constitutive properties of the workpiece material, which control plastic flow, strain hardening, and heat generation; (iii) cutting fluid and the resulting fluid flow, lubrication and cooling capacity; and (iv) the instantaneous wear state of the tool, which continually alters the actual cutting geometry, contact area, local stresses, and the generated forces and heat [15]. When process conditions and tooling are kept constant (as during this experimental work), the thermo-mechanical loads in the cutting zone are primarily influenced by the workpiece mechanical response and thermal properties [44]. The influence of mechanical properties arises because up to about 90% of the mechanical work in machining is converted into heat within the primary and secondary shear zones [46]. The thermal properties, in particular thermal conductivity, determine how much of the generated heat can be conducted away from the cutting zone into the chip and/or the generated workpiece surface. Accordingly, a material with lower thermal conductivity but otherwise identical properties would lead to higher cutting temperatures during machining.

In this work, as discussed above, similar cutting-force levels were measured for all three materials. To assess whether differences in thermal conductivity might nevertheless have contributed to the observed differences in tool wear, one must look at the thermal conductivities of wrought and AM 316L, see Table 5. At room temperature, the reported thermal conductivity of wrought 316L stainless steels is around 14 W/(mK) [47]. The data published on AM 316L is limited. Simmons et al. [48] reported thermal conductivity of PBF-LB/316L around 14.3 W/(mK) for dense material with porosity below 0.40%; only when porosity exceeded 2% were notable decreases in thermal conductivity observed. For DED-LB/316L Halmešová et al. [49] reported a thermal conductivity of 15.5 W/(mK), although no porosity data were provided for the measured samples. Taken together, these values suggest that the equivalent thermal loads in the cutting zone are in similar ranges. Under the identical cutting conditions used in this study, the resulting thermal loads in the cutting zone are therefore expected to be broadly comparable for all three workpiece materials.

In summary, mechanical (cutting force) and thermal (thermal conductivity-based) considerations suggest similar overall thermo-mechanical loads on cutting tools when machining the three 316L variants. These considerations alone cannot account for the observed differences in tool wear rates.

### 4.3. Abrasiveness of workpiece materials

One common source of abrasive wear found in many types of steels is hard carbides. In the concerned 316L stainless steel, however, no carbides were observed in any of the workpieces, which is consistent with the very low carbon content of this steel grade and its limited tendency to form carbides under the material-processing conditions used.

**Table 5**
Reported thermal conductivity for 316L [47–49].

| Processing method | Thermal conductivity (W/(mK)) |
|---|---|
| PBF-LB | 14.3 |
| DED-LB | 15.5 |
| Wrought | 14.0 |

Apart from carbides, hard non-metallic inclusions are well known to affect tool wear in machining [50,51]. In the present study, the observed differences in inclusion amounts and their properties are therefore likely to contribute to the tool wear.

Compared with the wrought workpiece, machining of the PBF-LB and DED-LB workpieces is expected to be associated with more pronounced abrasive tool wear, contributing to the faster flank-wear progression when machining these materials. There are two main reasons for this behavior. First, no machinability-enhancing MnS inclusions were found in the PBF-LB and DED-LB workpieces. Second, both AM materials contain substantially larger number and fraction of oxides than the wrought material, with this effect being especially pronounced for DED-LB, where the highest content of oxides was found. The larger population of hard oxide particles increases the likelihood of abrasion at the cutting interfaces and thereby intensifies abrasive wear. The latter behavior was also demonstrated by Hrechuck et al. [52] who created 316L workpieces with carefully controlled levels of oxides. Their machinability testing revealed a correlation between abrasive tool wear and the quantity of oxide particles present in the workpiece.

It is generally accepted that the process (material-fabrication) conditions characteristic of PBF-LB and DED-LB give rise to elevated levels of oxygen in the printed metal compared with conventional wrought material [19,20]. As possible oxygen sources, Deng [53] points to thin oxide layers present on feedstock powder particles. In addition, oxygen remnants in the process atmosphere can react with the hot metal in the melt pool and with ejected spatter particles, leading to incorporation of oxides into the solidified material [53].

For 316L steel in particular, Fig. 16 summarizes reported oxygen concentrations for PBF-LB, DED-LB and wrought material. The considerable scatter in reported values reflects differences in process conditions, including printing parameters, alloy batches, powder/feedstock handling across specific studies. However, two trends are clearly evident: (i) AM-processed 316L generally exhibits higher oxygen contents than wrought material, and (ii) within AM-materials, reported oxygen levels for DED-LB tend to exceed those for PBF-LB. The oxygen contents measured in this work (Table 1) are consistent with these trends. The same hierarchy is reflected in the quantitative inclusion analysis (Table 3), where the area fraction of oxide inclusions in the investigated size range are significantly higher in the AM workpieces than in the wrought material, with the highest values again found for

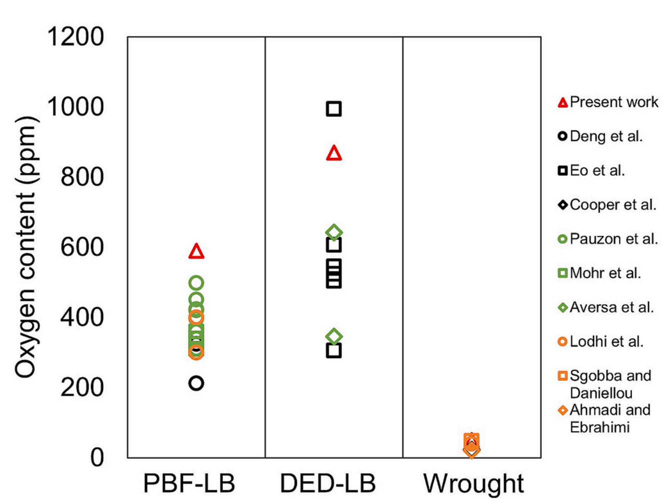


**Fig. 16.** Oxygen concentration reported for AM 316L stainless steel as compared to wrought material. Redrawn from [19,20,55–61].

DED-LB.

In contrast, the abrasive potential of non-metallic inclusions in the machinability-enhanced wrought 316L is expected to be significantly lower, and correspondingly the abrasive contribution to tool wear is comparably low. During the production of such machinability-enhanced grades, potentially hard, abrasive particles such as oxides are intentionally modified to reduce their hardness [54]. During conventional steelmaking, Mn added to the melt reacts with dissolved S to form MnS; these soft, ductile inclusions are widely considered to enhance machinability because they can act as solid lubricants and reduce friction and wear of the cutting tools. Consistent with this, significant fractions of MnS inclusions were found in the wrought workpiece.

No similar treatment for machinability-enhancement was applied to the AM workpieces. The oxide inclusions found in PBF-LB and DED-LB 316L are therefore expected to be harder than the Ca-modified oxides in the wrought material (see Fig. 8a). This combination – higher oxygen content, a larger fraction/density of hard oxides, and lack of MnS – significantly increases the abrasive potential of the AM materials during machining.

To summarize, the results indicate that abrasive wear in the PBF-LB and especially the DED-LB workpieces is a major contributor to the increased flank-wear rate when machining these materials in contrast to the machinability-enhanced wrought 316L where softer inclusions and a lower oxide content significantly reduce abrasive loading on the tool.

## 5. Summary and conclusions

Controlled turning tests combined with SEM, EDS, and EBSD characterization demonstrated that additively manufactured 316L produced by PBF-LB and DED-LB exhibits fundamentally different microstructures from wrought 316L. Compared with wrought material, both AM variants contained hierarchical columnar grain structures, higher crystallographic misorientation, and substantially larger amounts of oxide inclusions, while machinability-enhancing MnS inclusions were absent.

Although the three materials generated similar cutting forces under identical cutting conditions, the AM materials were characterized by accelerated flank wear and reduced tool life. The results indicate that these differences were not primarily governed by different thermo-mechanical loads during cutting, but rather by AM-induced microstructural characteristics, particularly the higher density of hard oxide inclusions together with the absence of machinability-enhancing MnS inclusions.

The findings demonstrate that inclusion characteristics should be considered alongside grain size, grain morphology, crystallographic texture, and hardness when evaluating and optimizing machinability of additively manufactured 316L. From an industrial perspective, the results suggest that improved oxygen control, reduced oxide formation, and adaptation of inclusion-engineering concepts to AM materials may provide viable routes for improving tool life and machining efficiency during post-processing.

Future work should further quantify the influence of specific microstructural parameters such as inclusion type and density, dislocation density, and grain size, on chip formation, surface integrity, and wear mechanisms to support the development of AM alloys optimized for both printability and machinability.

## CRediT authorship contribution statement

**Philipp Hoier:** Writing – original draft, Visualization, Supervision, Methodology, Investigation, Formal analysis. **Sri Bala Aditya Malladi:** Writing – review & editing, Visualization, Investigation, Formal analysis. **Dinesh Mallipeddi:** Supervision, Methodology, Investigation, Conceptualization. **Lars Nyborg:** Writing – review & editing, Project administration, Funding acquisition. **Peter Krajnik:** Writing – review & editing, Project administration, Funding acquisition, Formal analysis.

## Declaration of Generative AI and AI-assisted technologies in the writing process

During the preparation of this work, the author(s) used ChatGPT (OpenAI) to assist with structuring the manuscript, improving clarity, and enhancing the overall readability of the text. After using this tool/service, the author(s) critically reviewed, revised, and edited all content as necessary and take(s) full responsibility for the content of the published article.

## Declaration of competing interest

The authors declare that they have no known competing financial interests or personal relationships that could have appeared to influence the work reported in this paper.

## Acknowledgments

This research was supported by Sweden's innovation agency (Vinnova) under project 2018-05292, “Innovative Powder-based Components via Additive Manufacturing – Global Initiative (INNOGLOBE)” The authors thank Amir Malakizadi and Romain Mathieu for their valuable input and support during this study.

## References

[1] Meng W, Jia L, Pan Q, Li T, Liu G, Ma Q, et al. Breaking strength-ductility trade-offs in 316L stainless steel via oscillating wire arc additive manufacturing with nitrogen supersaturation. J Mater Process Technol 2025;346:119111. https://doi.org/10.1016/j.jmatprotec.2025.119111.

[2] Yi H, Jia L, Ding J, Li H. Achieving material diversity in wire arc additive manufacturing: leaping from alloys to composites via wire innovation. Int J Mach Tools Manuf 2024;194:104103. https://doi.org/10.1016/j.ijmachtools.2023.104103.

[3] Ma Z, Liu W, Li W, Song J, Liu H, Lv Z, et al. Microstructure evolution, composition distribution, and crack formation mechanisms of SS 316L/IN718 graded materials fabricated by laser directed energy deposition. J Mater Process Technol 2025;340:118843. https://doi.org/10.1016/j.jmatprotec.2025.118843.

[4] Cao Y, Moumni Z, Zhu J, Gu X, Zhang Y, Zhai X, et al. Effect of scanning speed on fatigue behavior of 316L stainless steel fabricated by laser powder bed fusion. J Mater Process Technol 2023;319:118043. https://doi.org/10.1016/j.jmatprotec.2023.118043.

[5] Dai R, Yang B, Wudy K. Impact of beam shaping on melt pool behavior in laser processing of stainless steel 316L: thermal analysis using multispectral imaging. J Mater Process Technol 2025;340:118835. https://doi.org/10.1016/j.jmatprotec.2025.118835.

[6] Qi H, Huang Z, Yang Z, Deng J, Chen Z, Wang J, et al. A novel pathway to realize the columnar-to-equiaxed transition and mechanical anisotropy suppression in SEBM of 316L. J Mater Process Technol 2026;347:119155. https://doi.org/10.1016/j.jmatprotec.2025.119155.

[7] Frazier WE. Metal additive manufacturing: a review. J Mater Eng Perform 2014;23:1917–28. https://doi.org/10.1007/s11665-014-0958-z.

[8] Vafadar A, Guzzomi F, Rassau A, Hayward K. Advances in metal additive manufacturing: a review of common processes, industrial applications, and current challenges. Appl Sci 2021;11:1213. https://doi.org/10.3390/app11031213.

[9] Gundgire T, Santa-aho S, Rautio T, Järvenpää A, Vippola M. Synergistic effects of heat treatments and severe shot peening on residual stresses and microstructure in 316L stainless steel produced by laser powder bed fusion. J Mater Process Technol 2024;323:118229. https://doi.org/10.1016/j.jmatprotec.2023.118229.

[10] Deng W, Wang C, Lu H, Meng X, Wang Z, Lv J, et al. Progressive developments, challenges and future trends in laser shock peening of metallic materials and alloys: a comprehensive review. Int J Mach Tools Manuf 2023;191:104061. https://doi.org/10.1016/j.ijmachtools.2023.104061.

[11] Maleki E, Bagherifard S, Bandini M, Guagliano M. Surface post-treatments for metal additive manufacturing: Progress, challenges, and opportunities. Addit Manuf 2021;37:101619. https://doi.org/10.1016/j.addma.2020.101619.

[12] Hoier P, Santhosh DK, Hryha E, Krajnik P. An investigation into the grindability of additively manufactured 42CrMo4 steel. CIRP Ann 2024;73:257–60. https://doi.org/10.1016/j.cirp.2024.04.039.

[13] Gunnerek R, Soundarapandiyan G, Mishurova T, Schröder J, Bruno G, Boykin J, et al. Chemical mechanical polishing of powder bed fusion – laser beam processed 316 L stainless steel. J Mater Process Technol 2025;345:119055. https://doi.org/10.1016/j.jmatprotec.2025.119055.

[14] Han W, Fang F. Fundamental aspects and recent developments in electropolishing. Int J Mach Tools Manuf 2019;139:1–23. https://doi.org/10.1016/j.ijmachtools.2019.01.001.

[15] Liao Z, Schoop JM, Saelzer J, Bergmann B, Priarone PC, Splettstößer A, et al. Review of current best-practices in machinability evaluation and understanding for

improving machining performance. CIRP J Manuf Sci Technol 2024;50:151–84. https://doi.org/10.1016/j.cirpj.2024.02.008.
[16] Guo P, Zou B, Huang C, Gao H. Study on microstructure, mechanical properties and machinability of efficiently additive manufactured AISI 316L stainless steel by high-power direct laser deposition. J Mater Process Technol 2017;240:12–22. https://doi.org/10.1016/j.jmatprotec.2016.09.005.
[17] Kitay O, Kaynak Y. Analysis of cutting tool geometry induced machining response, surface integrity and anisotropy relation of additively manufactured 316L stainless steel. J Manuf Process 2024;120:719–32. https://doi.org/10.1016/j.jmapro.2024.04.054.
[18] Li J, Gao D, Liao Z, Yang X, Zeng Y, Zan S, et al. The influence of material anisotropy on the machinability of laser additive manufactured stainless steel 316L. J Manuf Process 2025;145:581–99. https://doi.org/10.1016/j.jmapro.2025.04.056.
[19] Deng P, Karadge M, Rebak RB, Gupta VK, Prorok BC, Lou X. The origin and formation of oxygen inclusions in austenitic stainless steels manufactured by laser powder bed fusion. Addit Manuf 2020;35:101334. https://doi.org/10.1016/j.addma.2020.101334.
[20] Eo D-R, Park S-H, Cho J-W. Inclusion evolution in additive manufactured 316L stainless steel by laser metal deposition process. Mater Des 2018;155:212–9. https://doi.org/10.1016/j.matdes.2018.06.001.
[21] Ramalingam S, Watson JD. Inclusion chemistry control for machinability enhancement in steels. Mater Sci Eng 1980;43:101–8. https://doi.org/10.1016/0025-5416(80)90136-6.
[22] Helle A. On the interaction between inclusions in steel and the cutting tool during machining. 1995.
[23] Ånmark N, Karasev A, Jönsson P. The effect of different non-metallic inclusions on the machinability of steels. Materials 2015;8:751–83. https://doi.org/10.3390/ma8020751.
[24] Bletton O, Duet R, Pedarre P. Influence of oxide nature on the machinability of 316L stainless steels. Wear 1990;139:179–93. https://doi.org/10.1016/0043-1648(90)90044-B.
[25] Hoier P, Malakizadi A, Friebe S, Klement U, Krajnik P. Microstructural variations in 316L austenitic stainless steel and their influence on tool wear in machining. Wear 2019;428–429:315–27. https://doi.org/10.1016/j.wear.2019.02.024.
[26] Du H, Karasev AV, Jönsson PG. Influence of non-metallic inclusions in 316L stainless steels on machining using different cutting speeds. ISIJ Int 2021;61:2426–34. https://doi.org/10.2355/isijinternational.ISIJINT-2021-079.
[27] ISO/IEC 17025:2017 General requirements for the competence of testing and calibration laboratories n.d.
[28] ASTM E572–-21 Standard Test Method for Analysis of Stainless and Alloy Steels by Wavelength Dispersive X-Ray Fluorescence Spectrometry n.d.
[29] StTM E1086–-22 Standard Test Method for Analysis of Austenitic Stainless Steel by Spark Atomic Emission Spectrometry n.d.
[30] ASTM E1019–-24 Standard Test Methods for Determination of Carbon, Sulfur, Nitrogen, and Oxygen in Steel, Iron, Nickel, and Cobalt Alloys by Combustion and Inert Gas Fusion Techniques n.d.
[31] ISO 3685:1993 Tool-life testing with single-point turning tools n.d.
[32] Bachmann F, Hielscher R, Schaeben H. Texture analysis with MTEX – free and open source software toolbox. Solid State Phenom 2010;160:63–8. https://doi.org/10.4028/www.scientific.net/SSP.160.63.
[33] Bhadeshia HKDH. Steels: Microstructure and properties. 2006.
[34] DebRoy T, Wei HL, Zuback JS, Mukherjee T, Elmer JW, Milewski JO, et al. Additive manufacturing of metallic components – process, structure and properties. Prog Mater Sci 2018;92:112–224. https://doi.org/10.1016/j.pmatsci.2017.10.001.
[35] DebRoy T, Mukherjee T, Milewski JO, Elmer JW, Ribic B, Blecher JJ, et al. Scientific, technological and economic issues in metal printing and their solutions. Nat Mater 2019;18:1026–32. https://doi.org/10.1038/s41563-019-0408-2.
[36] Chechik L, Todd I. Inconel 718 two ways: powder bed fusion vs. directed energy deposition. Addit Manuf Lett 2023;6:100145. https://doi.org/10.1016/j.addlet.2023.100145.
[37] Bertsch KM, Meric de Bellefon G, Kuehl B, Thoma DJ. Origin of dislocation structures in an additively manufactured austenitic stainless steel 316L. Acta Mater 2020;199:19–33. https://doi.org/10.1016/j.actamat.2020.07.063.
[38] Gao L, Chen Y, Zhang X, Agnew SR, Chuang AC, Sun T. Evolution of dislocations during the rapid solidification in additive manufacturing. Nat Commun 2025;16:4696. https://doi.org/10.1038/s41467-025-59988-5.
[39] Wang YM, Voisin T, McKeown JT, Ye J, Calta NP, Li Z, et al. Additively manufactured hierarchical stainless steels with high strength and ductility. Nat Mater 2018;17:63–71. https://doi.org/10.1038/nmat5021.
[40] Leicht A, Klement U, Hryha E. Effect of build geometry on the microstructural development of 316L parts produced by additive manufacturing. Mater Charact 2018;143:137–43. https://doi.org/10.1016/j.matchar.2018.04.040.
[41] Lee S, Ghiaasiaan R, Gradl PR, Shao S, Shamsaei N. Additively manufactured 316L stainless steel via laser powder directed energy deposition (LP-DED): mechanical properties at cryogenic and elevated temperatures. Int J Fatigue 2024;182:108197. https://doi.org/10.1016/j.ijfatigue.2024.108197.
[42] Yan F, Xiong W, Faierson E, Olson GB. Characterization of nano-scale oxides in austenitic stainless steel processed by powder bed fusion. Scr Mater 2018;155:104–8. https://doi.org/10.1016/j.scriptamat.2018.06.011.
[43] Kim HS, Lee H-G, OH K-S. Precipitation behavior of MnS on oxide inclusions in Si/Mn deoxidized steel. Met Mater 2000;6:305–10. https://doi.org/10.1007/BF03028076.
[44] Malakizadi A, Mallipeddi D, Dadbakhsh S, M'Saoubi R, Krajnik P. Post-processing of additively manufactured metallic alloys – a review. Int J Mach Tools Manuf 2022;179:103908. https://doi.org/10.1016/j.ijmachtools.2022.103908.
[45] Malakizadi A, Saelzer J, Berger S, Alammari Y, Biermann D. A physics-based constitutive model for machining simulation of Ti-6Al-4V titanium alloy. Procedia CIRP 2023;117:335–40. https://doi.org/10.1016/j.procir.2023.03.057.
[46] Klocke Fritz. Manufacturing processes 2. 1st ed. Berlin, Heidelberg: Springer; 2009.
[47] Kim Choong S. Thermophysical properties of stainless steel. Argonne, Illinois: Argonne National Laboratory; 1975.
[48] Simmons JC, Chen X, Azizi A, Daeumer MA, Zavalij PY, Zhou G, et al. Influence of processing and microstructure on the local and bulk thermal conductivity of selective laser melted 316L stainless steel. Addit Manuf 2020;32:100996. https://doi.org/10.1016/j.addma.2019.100996.
[49] Halmešová K, Trojanová Z, Koukolíková M, Brázda M, Džugan J, Huang W. Effect of laser power on thermal properties of multimaterial structure Inconel 718 and stainless steel 316L processed by directed energy deposition. J Alloys Compd 2022;927:167082. https://doi.org/10.1016/j.jallcom.2022.167082.
[50] Hoier P, Malakizadi A, Klement U, Krajnik P. Characterization of abrasion- and dissolution-induced tool wear in machining. Wear 2019;426–427:1548–62. https://doi.org/10.1016/j.wear.2018.12.015.
[51] Binder M, Klocke F, Doebbeler B. Abrasive wear behavior under metal cutting conditions. Wear 2017;376(377):165–71. https://doi.org/10.1016/j.wear.2017.01.065.
[52] Hrechuk A, Slipchenko K, Maistro G, Bushlya V. Quantification of tool wear mechanisms in machining: the case of controlled-microstructure AISI 316L. Wear 2025;570:205944. https://doi.org/10.1016/j.wear.2025.205944.
[53] Deng Pu. The origins of nanoscale oxide inclusion and its evolution in additively manufactured austenitic stainless steel during laser powder bed fusion and post heat treatment. Auburn University; 2020.
[54] Larsson A, Ruppi S. Structure and composition of built-up layers on coated tools during turning of ca-treated steel. Mater Sci Eng A 2001;313:160–9. https://doi.org/10.1016/S0921-5093(01)00964-9.
[55] Cooper AJ, Cooper NI, Dhers J, Sherry AH. Effect of oxygen content upon the microstructural and mechanical properties of type 316L austenitic stainless steel manufactured by hot isostatic pressing. Metall Mater Trans A 2016;47:4467–75. https://doi.org/10.1007/s11661-016-3612-6.
[56] Pauzon C, Hryha E, Forêt P, Nyborg L. Effect of argon and nitrogen atmospheres on the properties of stainless steel 316 L parts produced by laser-powder bed fusion. Mater Des 2019;179:107873. https://doi.org/10.1016/j.matdes.2019.107873.
[57] Mohr G, Sommer K, Knobloch T, Altenburg SJ, Recknagel S, Bettge D, et al. Process induced preheating in laser powder bed fusion monitored by thermography and its influence on the microstructure of 316L stainless steel parts. Metals 2021;11:1063. https://doi.org/10.3390/met11071063.
[58] Aversa A, Saboori A, Librera E, De Chirico M, Biamino S, Lombardi M, et al. The role of directed energy deposition atmosphere mode on the microstructure and mechanical properties of 316L samples. Addit Manuf 2020;34:101274. https://doi.org/10.1016/j.addma.2020.101274.
[59] Lodhi MJK, Iams AD, Sikora E, Palmer TA. Microstructural features contributing to macroscopic corrosion: the role of oxide inclusions on the corrosion properties of additively manufactured 316L stainless steel. Corros Sci 2022;203:110354. https://doi.org/10.1016/j.corsci.2022.110354.
[60] Sgobba S, Daniellou T. Effects of thermocapillary forces during welding of 316L-type wrought, cast and powder metallurgy austenitic stainless steels. J Mater Process Technol 2003;143–144:578–83. https://doi.org/10.1016/S0924-0136(03)00373-X.
[61] Ahmadi E, Ebrahimi AR. Welding of 316L austenitic stainless steel with activated tungsten inert gas process. J Mater Eng Perform 2015;24:1065–71. https://doi.org/10.1007/s11665-014-1336-6.